Design of Au/Cdbr$_2$/Au as Negative Capacitance Devices and as Band Filters Suitable for 4G Technologies

A. F. Qasrawi[a,b]* ![ORCID], **Areen A. Hamarsheh**[a]

[a]Arab American University, Department of Physics, Jenin 240, Palestine.
[b]Istinye University, Department of Electrical and Electronics Engineering, 34010, Istanbul, Turkey.

Herein, cadmium bromide thin film devices are designed for possible use in communication technology. The 1.0 μm thin layer of CdBr$_2$ is sandwiched between two Au (1.0 μm thick) layers using the thermal evaporation technique under a vacuum pressure of 10^{-5} mbar. The Au/CdBr$_2$/Au devices are structurally morphologically and electrically characterized. It is observed that the hexagonal cadmium bromide exhibits large lattice mismatches with cubic Au substrates. The randomly distributed nano-rod like grains is accompanied with average surface roughness of ~26 nm. When an ac signal of low amplitude is imposed between the terminals of the Au/CdBr$_2$/Au devices, a negative capacitance effect in the frequency domain of 10-1800 MHz is observed. In addition, analysis of the impedance spectra in the same domain has shown that the device behaves as band pass/stop filters suitable for 4G technology. The microwave based standard analysis of the Au/CdBr$_2$/Au band filters have shown that it displays a notch (f_{co}) frequency of 2.0 GHz. The cutoff frequency at f_{co} reaches 7.86 GHz. The features of the Au/CdBr$_2$/Au devices nominate it for use as microwave resonators and as negative capacitance devices suitable for; 4G technology, noise reduction and for parasitic capacitance cancellation.

Keywords: *CdBr$_2$, 4G band filter, negative capacitance, microwave resonators.*

1. Introduction

Cadmium bromide compound capture the interest of researchers due to its nature of applications. It has great potential for lasing applications[1]. This compound is used for the enhancement of the efficiency of CdTe solar cells[2]. It is mentioned that the treatment of CdTe with a CdBr$_2$ increases the efficiency up to 8.6%. The associated short circuit current density and open circuit voltage reached a 23.7 mA/cm^2 and 0.76 V, respectively[2]. In addition, Ag doped CdBr$_2$ is mentioned being sensitive to the high energy photons like X-rays and ultra-violets. Such property of the material is advantageous as it leads to the enhancement of the optical density in CdBr$_2$ during chemical reactions[3].

CdBr$_2$ thin films of thickness of 4-30 nm are prepared from the aqueous solution by very slow evaporation (100 nm/h) of the solutes[4]. These films are mentioned exhibiting single crystalline nature. In addition, Mn-doped CdS/CdBr$_2$ hetero-nanostructures were prepared by the one step chemical vapor deposition technique[1]. Various methods have been employed to enhance the performance of CdBr$_2$ thin films. As for examples, the participation of silver ions in the structure of CdBr$_2$ is observed to enhance the light absorption in the crystals[5]. In another work, the phototreatment using bicolor coherent laser pulses of wavelengths of 1540 and 770 nm, it was possible to stimulate the linear electrooptical effects in CdBr$_2$/Cu nanocomposites[6]. The application of CdBr$_2$ in many technological sectors other than communication technology, motivated us to explore its performance as an electronic

device suitable for microwaves sensing. For this reason, here in this work, we have grown thin layers of cadmium bromide onto gold substrates. The layers of CdBr$_2$ are prepared by the vacuum thermal evaporation technique. This technique is preferred because it has unique advantages like easy controlling of film thickness, flexibility to tune interfaces, low defect density and free of solvents[7].

The gold substrate is selected because it is supposed to form rectifying contact with CdBr$_2$. Gold also displays smooth surfaces with roughness percentages of ~10% (experimentally determined). Such property makes signal propagation through electronic devices exhibit low loss factors. The produced Au/CdBr$_2$/Au devices will be structurally, morphologically, and electrically characterized. An ac signal of low amplitude will be imposed between the terminals of the device to explore it is performance as microwave resonators. The impedance spectroscopy parameters like capacitance, conductivity, impedance and reflection coefficient parameters will also be reported to identify the operation range of the devices.

2. Experimental Details

CdBr$_2$ thin films of thicknesses of 1.0 μm are coated onto a 1.0 μm thick Au substrates. Both of the Golds and CdBr$_2$ thin films are grown onto ultrasonically and chemically cleaned glass slides in a vacuum evaporator (NORM-600 thermal evaporator) under a vacuum pressure of 10^{-5} mbar. The Au and CdBr$_2$ films are prepared in two different growth cycles. The thin film substrates were located 10 cm above

*e-mail: atef.qasrawi@istinye.edu.tr

the CdBr$_2$ sources (powders of 99.0%, purity). Tungsten boats were used as heating sources for the evaporation of the films. The source temperature was kept at ~350 °C during the evaporation cycle of CdBr$_2$ and at ~1200 °C. The surface of Au/CdBr$_2$ was recoated with rectangular Au pads of areas of 3.14×10^{-2} cm^2. The thickness of the Au pads was also 1.0 μm. The films thicknesses were measured with the help of an in situ high resolution (0.03 $Å$) Inficon STM-2 thickness monitors. The thickness of the films was also tested with an SOLID IN II roughness monitor/profilometer. The structural measurements were carried out with the help of Minflex-600 X-ray diffraction (XRD) unit. The scanning speed was 0.5°/min. XRD measurements were carried out in the diffraction angle range of 10-70° using the $\theta - 2\theta$ scanning method. The surface morphology was tested with COXEM 200 scanning electron microscopes. The conductivity type of the CdBr$_2$ films were tested with the hot probe technique. The conductance, the capacitance and the impedance spectra were recorded with the help of Agilent 4291B 1.0M- 1.8 GHz impedance analyzer.

3. Results and Discussions

3.1. Design considerations

As confirmed by the hot probe technique, cadmium bromide thin films coated onto glass substrates reveal $p -$ type semiconductor characteristics. The electron affinity (qχ) and energy band gap (E_g) of p-CdBr$_2$ is 3.27 eV (ΔH_f^o for CdBr$_2$ is 314.6 kJ/mol corresponding to 3.27 eV[8]) and 3.21-3.30 eV, respectively[9]. Information about the position of the Fermi level (E_F) is rare. The only available information is about the thermal activation energy (0.40 eV[10]). Considering the thermal activation energy to be originating from the acceptors levels (caused by defects and un-purposely doped impurities) in the CdBr$_2$ samples, the

Fermi level position is then centered at 0.20 eV above the valence band ($E_v - E_F$). The expected work functions turn out to be, $q\phi = q\chi + E_g - (E_V - E_F) = 6.37\text{-}6.27$ eV. For this reason, coating CdBr$_2$ films onto a face centered cubic gold whose work function is 5.34 eV[11] lead to the formation of Schottky type rectifying contacts. In addition, one should work with the warranty that the large lattice mismatches between the cubic Au substrates and the hexagonal CdBr$_2$ is expected to form a space charge layer at the ultrathin interfaces[12]. Interfaces due to lattice mismatches may also leads to the construction of the nano-heterojunctions[12]. Moreover, the surface roughness's of the stacked layers may also force to the formation of an interface space charge region[13]. For these reasons, in the following sections, we will consider the structure, the surface morphology and then, the electrical characterizations to check the Schottky property of the metal sandwiched structure.

3.2. Structural and morphological analyses

Figure 1 illustrates the X-ray diffraction results for the CdBr$_2$ coated onto Au substrates. The analysis of the sharp XRD patterns were carried out using "Crystdiff" and "TREOR 92" software packages in accordance with the available crystallography open database (COD) cards for Au (COD: 9008463) and for CdBr$_2$ (COD : 8104257). The data analyses indicated that the sharpest peak of the observed XRD patterns correspond to the hexagonal phase of CdBr$_2$ being oriented along the $c -$ axis in the (002) plane direction. The lattice parameters of the hexagonal phase of CdBr$_2$ are found to be $a = 3.985$ Å and $c = 12.561$ Å consistent with the published literature data[14]. It is also noticed that, the XRD patterns contained peaks that are assigned to cubic Au and the orthorhombic Au$_2$O$_3$[12]. The phase weight of Au$_2$O$_3$ ($Phase\% = \sum A_{Au2O3} / A_{All\ peaks}$; A is area) is 4.6%. The oxidation of gold could have resulted from the humidity conditions before the gold evaporation. It is
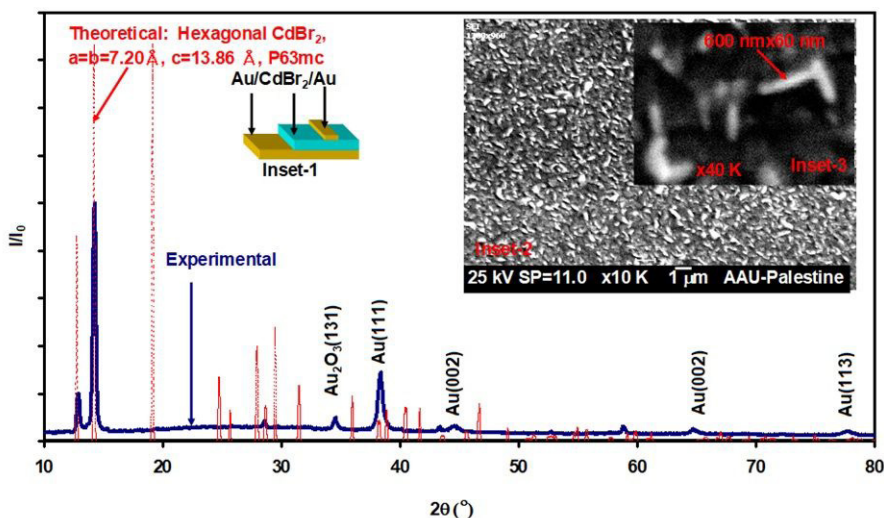

Figure 1. The X-ray diffraction patterns for Au/CdBr$_2$ thin films. Inset- 1 shows the geometrical design of the samples and inset- 2 and inset-3 illustrate the scanning electron microscopy images for the samples (grown onto glass) with images being enlarged 10,000 and 30,000 times, respectively. The dotted curve shows the theoretically estimated XRD patterns for the hexagonal CdBr$_2$.

also noticeable that the diffraction peak which appeared at $2\theta = 12.77^o$ does not relate to the assumed crystal structure with the lattice parameters be $a = 3.985$ Å and $c = 12.561$ Å. Various tests to explore the reason beyond the existence of this peak were carried out. The tests included the crystal structure of bromine, cadmium, CdO and Au_2Br_3. None of these crystal structures were related to the peak which is detected at $2\theta = 12.77^o$. Hence, we went to the belief that the preferred crystal structure has grown with different unit cell dimensions. We were able to execute an exact solution with unit cell parameters of $a = b = 7.20$ Å, $c = 13.86$ Å and space group of $P63mc$. The reflection peaks of this unit cell which reproduce the experimental data are shown by the red colored dashed lines in Figure 1. The theoretically estimated crystal data including diffraction angles with intensities and plane orientations are illustrated in Table 1. In accordance with the table, all the observed XRD peaks (shown by asterisks in the table) are correctly indexed. The peak which is observed at $2\theta = 12.77^o$ now indexed in the (002) plane orientation and the peak observed at $2\theta = 14.20^o$ is now indexed along the (010) planes. As the lattice parameters for the cubic Au which is best oriented along the (111) direction is 4.08 Å, the lattice mismatches[15] between the substrate and CdBr₂ along $c - axis$ ($\Delta\% = 100.\dfrac{|c_{CdBr2} - c_{Au}|}{c_{CdBr2}}$) is 67.5%. The lattice mismatches along the $a - axis$ is ~2.3%. These $\Delta\%$ values are determined assuming $a = b = 3.985 Å$ and $c = 12.561 Å$. On the other hand, the lattice mismatches between Au and CdBr₂ assuming the validity of the $a = b = 7.20 Å$, $c = 13.86 Å$ lattice parameters are $\Delta_a\% = 43.3\%$ and $\Delta_c\% = 70.5\%$.

On the other hand, the surface morphology analysis which was carried out with the help of scanning electron microscopy (SEM) for CdBr₂ samples grown onto glass substrates reveals none uniform random distribution of a rod like grains. The grains which are illustrated in inset- 2 and inset- 3 of Figure 1 exhibit length of 600-1500 nm and width of 60-130 nm. In general, grains are composed of collection of small crystallites[16,17]. The crystallite sizes are determined from the XRD patterns. Our investigations on the crystallites sizes

of the formed Au/CdBr₂ interfaces using Scherrer equation ($D = \dfrac{0.94\lambda}{\beta\cos(\theta)}$; β peak broadening[11,17]) revealed values of 28 nm. The microstrain ($\varepsilon = \beta / (4\tan(\theta)^{17})$) is found to be 10.47×10^{-3} leading to a defect density ($\delta = 15\varepsilon / (cD)^{17}$) of 7.86×10^{11} lines/cm². Compared to other nanoscale materials[17,18], the defect density of CdBr₂ films is comparable. The lower the dislocation line density, the lower the defect density, the higher the crystallinity[18].

Additional surface morphology test was carried out with the help of a profilometer. The obtained average surface roughness was 26 nm. The root mean square value along the sampling length is 50 nm. The ratio of the average roughness to the film's thickness is 5.2%. This value indicate that the film surface is smooth. Roughness percentages of 28.4% was previously observed for Au/Bi₂O₃ interfaces[11]. This value was large enough to block the formation of Schottky barrier at the Au/Bi₂O₃ interfaces. While roughness percentages of 10.9% allowed the formation of Schottky barriers at Yb/Bi₂O₃ interfaces[11]. Other studies have shown that CdBr₂ usually exhibit, low roughness values. It is mentioned that the uniform thickness and smooth flat surface along the growth direction of the films provides a basis for the high-speed migration of carriers in one dimension[9].

3.3. Direct and alternating current conduction mechanisms

For the Au/CdBr₂/Au devices whose geometrical design is shown in inset-2 of Figure 1, the dc current-voltage characteristics is shown in the inset of Figure 2a. The figure display, weak rectifying nature of Schottky barriers. The lack of well rectifying properties of the designed diodes is assigned to the large number of surface defect centers (7.86×10^{11} lines/cm²). In general, the surface effect on metal/semiconductor interfaces are primarily attributed to the ionic charges on or outside the semiconductor surface. These charges induces image charges in the semiconductor, and thereby cause the formation of the so-called surface channels or surface depletion-layer regions[15]. Once a channel

Table 1. the theoretical crystal diffraction data for hexagonal CdBr₂ being calculated for lattice parameters of $a = b = 7.20 Å$, $c = 13.86 Å$, space group $P63mc$.

| $2\theta(^o)$	I/Imax	h k l	$2\theta(^o)$	I/Imax	h k l	$2\theta(^o)$	I/Imax	h k l
*12.76	100.00	0 0 2	31.44	15.50	0 2 2	49.04	2.90	0 2 6
*14.19	77.50	0 1 0	35.94	9.60	1 -2 4	50.79	1.30	2 2 0
*19.13	71.90	0 1 2	36.02	9.50	2 -1 4	51.21	2.40	0 3 4
24.71	17.10	1 -2 0	38.28	3.80	2 1 0	52.94	1.10	1 3 0
25.69	15.20	0 0 4	40.57	6.10	3 -1 2	53.10	1.00	3 1 0
27.90	23.20	1 -2 2	41.68	5.50	1 0 6	54.70	1.90	1 3 2
*28.61	10.70	0 2 0	*43.71	2.30	3 0 0	55.70	1.70	1 2 6
29.47	19.40	0 1 4	45.52	3.90	0 3 2	57.77	1.50	2 2 4
29.48	19.40	1 -1 4	46.61	3.50	1 2 4	*59.16	1.40	1 1 8

*coincides with experimental data
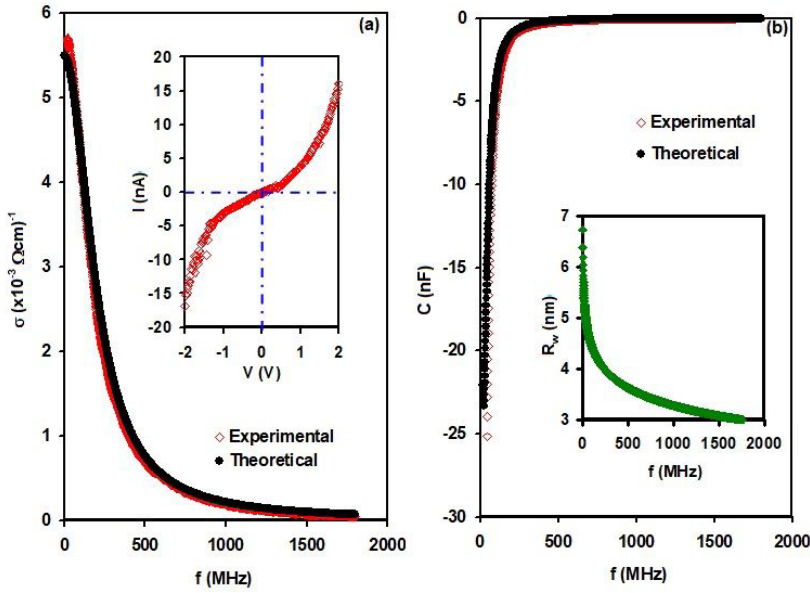
Figure 2. (a) the conductivity and (b) the capacitance spectra for Au/CdBr$_2$/Au devices. The inset of (a) shows the dc current-voltage characteristics curve and inset of (b) shows the frequency dependence of average hopping distance.

is formed, it modifies the Schottky depletion region and gives rise to surface leakage current[15].

The alternating current measurements revealed the conductivity (σ) and the capacitance (C) spectra that are shown in Figure 2a and b, respectively. The spectral measurements are carried out in the frequency (f) domains of 10-1800 MHz. It is clear from Figure 2a that the conductivity sharply decreases with increasing signal frequency. It decreases by more than two orders of magnitude as the signal frequency increases from 10 MHz to 1800 MHz. The decaying conductivity provide information about the dominant current conduction mechanism in the samples. Our trails which included tests for possible domination of current conduction mechanisms arrived at the result that the most preferable conduction is by correlated barriers hopping (CBH) in which the conductivity takes the form[19-21],

$$\sigma_{CBH}(w) = \sigma(H) + \frac{\sigma(L) - \sigma(H)}{1 + \left(w\tau_{hop}\right)^2} \tag{1}$$

In CBH conduction, the frequency dependent hopping distance is given by,

$$R_w = \frac{1}{2\alpha} \ln\left(\frac{1}{w\tau_o}\right) \tag{2}$$

Here, τ_o is characteristic relaxation time which is the inverse of the phonon frequency ($\upsilon = \tau_o^{-1}$), α^{-1} is the spatial decay parameter which describes the localized states at each site and is constant for all sites ($\alpha^{-1} \sim 10\,\mathring{A}$). In Equation 1; $\tau_{hop} = \tau_o \exp\left(\dfrac{E_H}{kT}\right)$ with E_H being the height of potential

Table 2. alternating current conduction parameters for CdBr$_2$ thin films.

Parameter	Value
$\tau_o\,(ps)$	0.23
$\tau_p = \tau_{hop}$ (ns)	5.0
ν (cm^{-1})	148
$\sigma(L) \times (10^{-3}\ \Omega^{-1}cm^{-1})$	5.5
$\sigma(H) \times (10^{-5}\ \Omega^{-1}cm^{-1})$	1.0
$E_H\,(eV)$	0.26
C_o (pF)	3.0
a_2 (F/s)	7.5
w_p (MHz)	90

barriers that the holes hope over. $\sigma(L)$ and $\sigma(H)$ are the low and high frequency conductivity values, respectively. Inserting the value of the phonon frequency as 148 cm^{-1}[22], with appropriate $\sigma(L)$ and $\sigma(H)$ and other related parameters. It is possible to reproduce the experimental conductivity spectra. The excellent correlation between the experimentally observed and theoretically produced using Equation 1-Equation 2 is shown by black solid circles in Figure 2a. The related fitting parameters are listed in Table 2.

The value of the phonon frequency being 148 cm^{-1} which was able to reproduce the experimental data was taken from the Raman spectroscopy measurements for CdBr$_2$[22]. The phonon oscillation which is assigned to A_{g1} modes was obtained from the observed first-order Raman and infrared lines in CdBr$_2$[22]. As the table shows, the hopping time constant

which is reached by this fitting procedure is 5.0 ns. Hence, the average correlated barrier height is 0. 26 eV. In addition, the average hopping distance which is frequency dependent is calculated with the help of Eqnation 2 and is displayed in the inset of Figure 2b. The higher the propagating signal frequency, the shorter the average hopping range. It indicates that the lack of long-range order will negatively affect the response of the CdBr$_2$ when used as time based sensors like microwave filters[23].

3.4. Negative capacitance effect

The first practical application for the Au/CdBr$_2$/Au layers appears in the measured capacitance spectra. The capacitance spectra which are illustrated in Figure 2b is negative indicating that the device under study could be employed as negative capacitance effect device. These classes of devices play important roles in communication technology. The negative capacitance (NC) effects devices are used as noise reducers, parasitic capacitance cancellers and as signal amplifiers[19,20,24]. NC effect is reported resulting from the depolarization field that produces a decreasing voltage across the capacitance while the induced charge is increasing[25]. It is also believed that the NC effect could have resulted from a minority charge injections caused by the accumulation of minority carriers at the crystallite boundaries[26]. Available models which take into account the minority carrier injection includes the Ershov-Qasrawi approach[19,20,27,28]. In this approach, the interpretation of NC is based on the analysis of the time-domain transient current in response to a small voltage step or impulse that includes a self consistent treatment of carrier transport, carrier injection and recharging. The total capacitance take the form,

$$C(w) = C_o + C_1 = C_o + \frac{a_n \tau_n}{1 + (w - w_n)^2 \tau_n^2} - \frac{a_p \tau_p}{1 + (w - w_p)^2 \tau_p^2} \quad (3)$$

In the above equation, the capacitance is composed of as the geometrical capacitance, and a relaxation part (C_1) that is caused by the electron transport, carrier injection, trapping, impact ionization, and other physical processes. In Equation 3 τ_n and τ_p are the relaxation times of electrons and holes, respectively. a_n and a_p are fitting parameters for the capacitance response resulting from dipole orientations during the electron-plasmon coupling process and hole-plasmon coupling processes, respectively. Since the hot probe technique showed p-type conductivity for CdBr$_2$ and the capacitance remained negative in all the studied frequency domain, the effect of minority carriers (electrons) on the NC effect is of less significance (cannot be observed). For this reason $a_n = 0 \text{F}/\text{s}$ is assumed. Thus, the capacitance spectra are reproduced from the dynamical part of holes. The good fitting of the experimental data which appears (black circles) in Figure 2b was achieved with the data listed in Table 2. The rate of change of capacitance due to holes injections with time (a_p) is 7.5 F/s. The hole-plasmon coupling frequency is found to be ~ 90 MHz. The relaxation times for holes being 5.0 ns is the same as that determined from the hopping mechanism of conductivity. This value represents the inverse of the electronic friction damping constant ($\gamma \propto \tau_p^{-1}$). This value is lower than the one we previously observed as 10 ns for CdS/Sb$_2$Te$_3$ heterojunction devices[28]. The shorter the relaxation time constant, the larger the electronic friction. Electronic friction arises from interfacial electronic interactions[29]. It could also arise from the excitation of electron- hole pairs in the metal (Au substrate)[30].

3.5. Microwave band filter characteristics

Figure 3a illustrates the impedance (Z) spectra for the Au/CdBr$_2$/Au devices. The impedance of the device smoothly increases with increasing signal frequency in the frequency domain of 10-1000 MHz. As the frequency exceeds 1000 MHz, the impedance sharply increases by
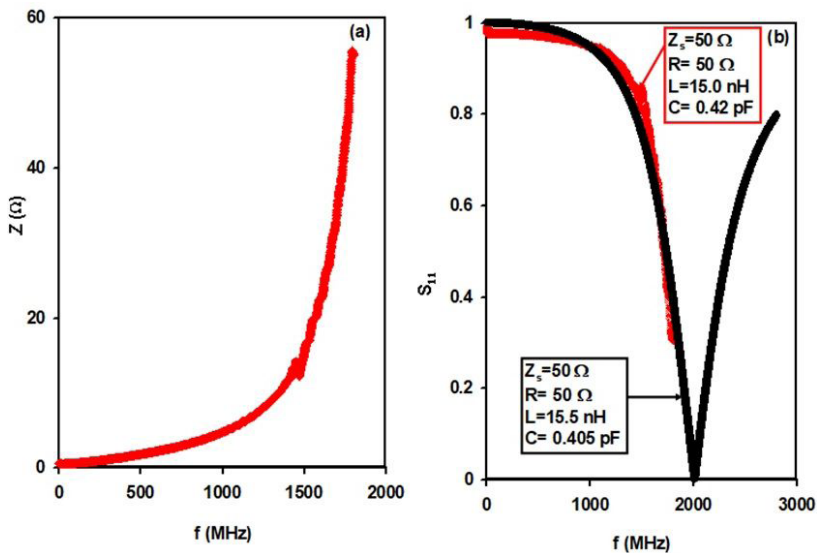

Figure 3. (a) the impedance and (b) the magnitude of the reflection coefficient parameters for Au/CbBr$_2$/Au thin films.

more than 10 times. The instrumental limitations (impedance analyzer work in the range of 10-1800 MHz) prohibited observation of the highest reachable impedance value. Recalling that the high impedance mode indicates that the device in the circuit allows a relatively small amount of current to pass through (per unit applied voltage at that point), then the device can be employed as band filters[31]. The type of band filters can be more visible though calculation of the magnitude of reflection coefficient

($\rho = \left| \dfrac{Z_{source} - Z_{Au/CdBr2/Au}}{Z_{source} + Z_{Au/CdBr2/Au}} \right|$) or calculation of the so

called S_{11} ($Z_{Au/CdBr2/Au} = \dfrac{1+S_{11}}{1-S_{11}} Z_{Source}$) parameter[31].

The spectral representation of this parameter is shown in Figure 3b. Values of S_{11} =0 indicate perfect math between the device and the source, while on the other hand values of S_{11} =1.0 means the impedance of the device is much larger than that of the source and the circuit is open. For the Au/CdBr$_2$/Au devices, S_{11} parameter exhibits values of ~1.0 in the frequency domain of 10-1200 MHz. When the propagating signal frequency exceeds this 1200 MHz, S_{11} spectra follow a decreasing trend of variation reaching minimum value at 1800 MHz which is the limit of our impedance analyzer. The lower the value of S_{11}, the better the match between sources and device. To explore the notch frequency of the proposed Au/CdBr$_2$/Au band filters which is beyond our instrument facility, we have reproduced the experimental spectra of S_{11} assuming a series RLC circuit. In this circuit, $Z_{Au/CdBr2//Au} = R + jwL - jwC.$ To reproduce the experimental data a simple simulator based on this equation was created. The simulator establish fitting parameters that relate to good correlation between the theoretical and experimental data. As can be seen from the Figure 3b, the values of R, L and C which reproduce the S_{11} spectra are 50 Ω, 15 nH and 0.42 pF, respectively. However, to reach an exactly zero value of S_{11}, the respective values of R, L and C should be 50 Ω, 15.5 nH and 0.405 pF. Using these values, the notch frequency of the Au/CdBr$_2$/Au band filters is 2.0 GHz. When the device exhibit R, L and C of values of be 50 Ω, 15.5 nH and 0.405 pF , respectively, perfect matches between the source and device can be achieved[26]. In addition, the microwave cut off frequency ($f_{co} = 1/(2\pi RC)$) for the Au/CdBr$_2$/Au at the notch frequency is 7.86 GHz. Both of the notches and the cut off frequency values are promising as they indicate the possibility of using the device under study as band stop filters suitable for 4G mobile technologies. Recent developments in the 4G technology indicated the production of band filters and microstrips[32]. In these designs, two varactor diodes and biasing circuit components were selected to produce tunable filters. The impedance bandwidth of this structure is kept between 95 and 115 MHz with measured return losses of more than 17 dB and measured insertion loss of less than 1 dB. In addition, the features of the currently reported Au/CdBr$_2$/Au devices are combatable with band stop filters (notch filters) proposed for fourth generation long term evolution (4G LTE) technology[33]. The anticipated conditions for the LTE band included a frequency domain

of 1.92-1.98 GHz. This system which is nominated for use in mobile phones is based on series-cascaded absorptive band stop filters that are adapted in the radio frequency spectrum to create the desired passband and out of band responses. The system included transmit and receive filters with low insertion loss (2.8-4.9 dB)[33]. Our band filters display characteristics close to those reported for compact planer openloop bandpass filters designed for 4G applications. These microstrip band pass filters use four open-loop ring resonators with 50 Ω tapped lines for input and output ports[34].

It is worthy of notifying that one may attempt to interpret the NC effect in terms of conventional inductance. This approach is not physically meaningful when the impedance resulting from inductance ($|Z| = \omega L$) increases with frequency and, therefore, should dominate at high frequencies. The increase in Z values with increasing signal frequency is read from Figure 3a. In our samples, the high-frequency capacitance is negative indicting the possible dominant of the parasitic inductance[27]. It is mentioned that when a negative capacitance is used instead of an inductance in the shunt circuit, the whole circuit are capacitive without resonance. However the voltage on the device can still be inverted effectively. The magnitude of voltage on the device terminals depends on the difference between the inherent capacitance of the device and the negative capacitance. Selecting proper negative capacitance values can lead to large magnitude of voltage allowing good control of the device[35].

4. Conclusions

In this work, we have reported the possible design of band pass/stop filters that suits 4G technology. The band filters employ CdBr$_2$ thin layer as dielectric media between two Au electrodes. It is observed that the Au/CdBr$_2$/Au devices could handle dual operations presented by negative capacitance effect and microwave band filter at the same time. The notch and cut off frequency value of the Au/CdBr$_2$/Au band pass filters reaches 2.0 and 7.86 GHz, respectively. The easy fabrication method, the small size of the thin film device ($A = 3.14 \times 10^{-2} cm^2$) and the critical electrical parameters of the device nominate it for use in microwave technology employed in mobiles and communication technology.

5. Acknowledgments

6. References

1. Zou S, Yang G, Pang T, Zou M, Liu R, Chen B, et al. One-step synthesis of nail-like Mn-doped CdS/CdBr2 hetero-nanostructures for potential lasing application. Nanotechnology. 2019;30(7):075605.

2. Greenhalgh RC, Tsai V, Abbas A, Kornienko V, Fiducia TAM, Togay M, et al. Analysis of MZO/CdTe photovoltaic device treated with cadmium bromide. In: 2019 IEEE 46th Photovoltaic

Specialists Conference (PVSC); 2019; Chicago, IL, USA. Proceedings. USA: IEEE; 2019. p. 2489-93.

3. Stetsyk NV, Antonyuk VG, Rudka MM. Title. J Nano- Electron Phys. 2014;6(2):02001.

4. Plucinski KJ, Lakshminarayana G. CdBr 2 nanocrystalline layers as nonlinear optical materials. J Mater Sci Mater Electron. 2013;24(12):5162-5.

5. Bellucci S, Bolesta I, Karbovnyk I, Kolych I, Martyniv S, Velgosh S. Influence of silver clusters on the light absorption in CdBr 2-Ag crystals. J Nanophotonics. 2010;4(1):049503.

6. Lakshminarayana G, El-Naggar AM, Myronchuk GL, Gondek E, Reshak AH, Czaja P, et al. Laser-stimulated Pockels effect in CdBr2/Cu polymer nanocomposites. Physica E. 2020;118:113904.

7. Wang S, Li X, Wu J, Wen W, Qi Y. Fabrication of efficient metal halide perovskite solar cells by vacuum thermal evaporation: a progress review. Current Opinion in Electrochemistry. 2018;11:130-40.

8. Ervin KM. Hydrocarbon radical thermochemistry: gas-phase ion chemistry techniques. USA: USDOE Office of Science; 2014. No. DOE-UNR-ER-15645. Board of Regents, Nevada System of Higher Education, on behalf of Univ. of Nevada, Reno, NV (United States).

9. Wang F, Jia L, Ding Y, Cai H, Zheng W, Huang F. Ultra-long van der waals CdBr2 micro/nanobelts. Small Methods. 2020;4(10):2000501.

10. Novosad SS, Gal'chynskyy OV, Kovalyuk RO. Effect of ultraviolet light irradiation on electrical properties of CdBr2: Cu+ single crystals. Nucl Instrum Methods Phys Res B. 1996;116(1-4):265-8.

11. Khusayfan NM, Qasrawi AF, Khanfar HK. Impact of Yb, In, Ag and Au thin film substrates on the crystalline nature, Schottky barrier formation and microwave trapping properties of Bi2O3 films. Mater Sci Semicond Process. 2017;64:63-70..

12. Wang M, Xu Y, Jin H, Li D. Effect of pn type nano-heterojunction formed between two narrow bandgap semiconductors in Cu+ doped GeSe2-Sb2Se3 glass ceramics on photocatalytic activities. Semicond Sci Technol. 2020;35(3):035017.

13. DeWames RE, Schuster J. Performance and limitations of NIR and extended wavelength eSWIR InP/InGaAs image sensors. In: SPIE OPTO, 2020. Quantum Sensing and Nano Electronics and Photonics XVII; 2020; San Francisco, California, United States. Proceedings. Bellingham: International Society for Optics and Photonics; 2020. vol. 11288, p. 112880H-14.

14. Mitchell RS. Single crystal X-ray study of structural polytypism in cadmium bromide. Z Kristallogr Cryst Mater. 1962;117(4):309-18.

15. Sze SM, Ng KK. Physics of semiconductor devices. Hoboken: John Wiley & Sons; 2021.

16. Freitas AE, Manhabosco TM, Batista RJC, Segundo AKR, Araújo HX, Araújo FGS, et al. Development and characterization of titanium dioxide ceramic substrates with high dielectric permittivities. Materials (Basel). 2020;13(2):386.

17. Qasrawi AF, Sahin Eİ, Abed TY, Emek M. Structural and dielectric properties of Ba1− xLax (Zn1/3Nb2/3) O3 solid solutions. Phys Status Solidi B. 2020:2000419.

18. Zhang W, Sun A, Zhao X, Pan X, Han Y, Suo N, et al. Structural and magnetic properties of Ni–Cu–Co ferrites prepared from sol-gel auto combustion method with different complexing agents. J Alloys Compd. 2020;816:152501.

19. Qasrawi AF. Characterization of Au/As2Se3 multifunctional tunneling devices. Phys Status Solidi A. 2020;217:(5):1900899.

20. Qasrawi AF, Zyoud HM. Fabrication of (Au, Mn)/ZnPc/Ag interfaces as radiowave/microwave band filters. Phys Status Solidi A. 2020;217(22):2000171.

21. Darwish AAA, El-Nahass MM, Bekheet AE. AC electrical conductivity and dielectric studies on evaporated nanostructured InSe thin films. J Alloys Compd. 2014;586:142-7.

22. Lockwood DJ. Lattice vibrations of CdCl 2, CdBr 2, MnCl 2, and CoCl 2: infrared and Raman spectra. JOSA. 1973;63(3):374-82.

23. Subahi AM, Griffiths JA, Mannan S, Boardman J, Moir-Riches P, Royle GJ. Assessment and development of novel transition metal oxide materials as a photovoltaic sensor. In: SPIE Photonics Europe, Optical Sensing and Detection; 2010; Brussels, Belgium. Proceedings. Bellingham: International Society for Optics and Photonics; 2010. vol. 7726, p. 77262E. http://dx.doi.org/10.1117/12.853745.

24. Gao T, Zeng L, Zhang D, Zhang Y, Wang KL, Zhao W. Compact model for negative capacitance enhanced spintronics devices. IEEE Trans Electron Dev. 2019;66(6):2795-801.

25. Zhou J, Han G, Xu N, Li J, Peng Y, Liu Y, et al. Experimental validation of depolarization field produced voltage gains in negative capacitance field-effect transistors. IEEE Trans Electron Dev. 2019;66(10):4419-24.

26. Wang K, Shen WZ, Yang HF. Capacitance characteristics in PbSrSe thin films. Appl Surf Sci. 2003;217(1-4):100-7.

27. Ershov M, Liu HC, Li L, Buchanan M, Wasilewski ZR, Jonscher AK. Negative capacitance effect in semiconductor devices. IEEE Trans Electron Dev. 1998;45(10):2196-206.

28. Khusayfan NM, Qasrawi AF, Khanfar HK. Design and electrical performance of CdS/Sb 2 Te 3 tunneling heterojunction devices. Mater Res Express. 2018;5(2):026303. Mater Res Express. 2018;5(2):026303.

29. Daly C, Krim J. Sliding friction of solid xenon monolayers and bilayers on Ag (111). Phys Rev Lett. 1996;76(5):803-6.

30. Smith BB, Hynes JT. Electronic friction and electron transfer rates at metallic electrodes. J Chem Phys. 1993;99(9):6517-30.

31. Pozar DM. Microwave engineering. Hoboken: John Wiley & Sons; 2011.

32. Al-Yasir YIA, Ojaroudi Parchin N, Tu Y, Abdulkhaleq AM, Elfergani ITE, Rodriguez J, et al. A varactor-based very compact tunable filter with wide tuning range for 4G and Sub-6 GHz 5G communications. Sensors (Basel). 2020;20(16):4538.

33. Psychogiou D, Mao R, Peroulis D. Series-cascaded absorptive notch-filters for 4G-LTE radios. In: 2015 IEEE Radio and Wireless Symposium (RWS); 2015; San Diego, CA, USA. Proceedings. USA: IEEE; 2015. p. 177-9.

34. Al-Yasir YIA, OjaroudiParchin N, Abdulkhaleq A, Hameed K, Al-Sadoon M, Abd-Alhameed R. Design, simulation and implementation of very compact dual-band microstrip bandpass filter for 4G and 5G applications. In: 2019 16th International Conference on Synthesis, Modeling, Analysis and Simulation Methods and Applications to Circuit Design (SMACD); 2019; Lausanne, Switzerland. Proceedings. USA: IEEE; 2019. p. 41-4.

35. Ji H, Qiu J, Cheng J, Inman D. Application of a negative capacitance circuit in synchronized switch damping techniques for vibration suppression. J Vib Acoust, 2011;133(4):041015.